NUMERICAL SIMULATION OF GAS DYNAMICS IN A BUBBLE DURING ITS COLLAPSE WITH THE FORMATION OF SHOCK WAVES

A. A. Aganin and M. A. Il'gamov   UDC 534.2:532

The specific features of calculation of a gas in a spherical bubble located in the center of a spherical volume of weakly compressible fluid are considered. The problems of motion of a cold gas to a point and a spherical piston converging to a point are used to evaluate the algorithm. It is shown that significant errors can arise in calculation of spherical waves in the vicinity of the pole. These errors can be substantially reduced by means of artificial viscosity in the Riemann problem.

Introduction. The problems of dynamics of a gas bubble in a fluid are usually addressed in studying the effect of cavitation on objects located in a fluid flow [1–3]. However, they are also of interest in connection with the phenomenon of one-bubble sonoluminescence [4], which is very promising for the development of physics and chemistry [5].

Until recently, in most models the expansion–compression of a gas in a bubble was assumed to be uniform, and the fluid surrounding the bubble was assumed to be incompressible or weakly compressible [1–3, 6–8]. These models work well as long as the bubble surface velocity remains subsonic. Otherwise, shock waves appear in the bubble, and the bubble dynamics becomes significantly different. A calculation with the use of hydrodynamic equations for modeling the gaseous medium of the bubble was performed for the first time by Wu and Roberts [9]. The fluid around the bubble was described in the same way as in models that lead to the Rayleigh–Plesset type equation. A similar approach was used by other authors [10, 11]. Moss et al. [12] used numerical integration of hydrodynamic equations both for the gas and for the fluid. At the same time, even the calculation of one oscillation requires significant computer time if one does not use simplifications taking into account the specific features of the solution behavior in space and time.

Numerical integration of gas-dynamic equations was performed by the Lax–Friedrichs method [9], using the software system DYNA2D [12], and also by solving the Riemann problem [10, 11]. The accuracy of the numerical solution depends to a large extent on how accurately this solution describes the shock waves converging to the pole, their interaction in the pole, and the shock waves diverging from this pole, which result from this interaction. This problem is not discussed in [9, 10, 12]. The specific features of numerical simulation of gas dynamics in a bubble during its collapse with the formation of shock waves are considered in the present paper on the basis of solving the Riemann problem. The problems of motion of a cold gas to a point and a spherical piston converging to a point are used to evaluate the algorithm.

Formulation of the Problem and Method of Solution. We consider gas dynamics in a spherical bubble located in the center of a spherical volume of a fluid. On the external side of this bubble, we specify the pressure

$$p_{\text{ex}}(t) = p^0 - \Delta p_{\text{ex}} \sin\left(\omega t\right), \tag{1}$$

where p^0 is the mean pressure, Δp_{ex} and ω are the amplitude and frequency of oscillations, and t is the time. At $t < 0$ the bubble and the fluid are at rest.

The gaseous medium in the bubble is described by the system of equations for a perfect gas with the van der Waals equation of state

$$\frac{\partial(\rho r^2)}{\partial t} + \frac{\partial(\rho r^2 u)}{\partial r} = 0, \qquad \frac{\partial(\rho r^2 u)}{\partial t} + \frac{\partial(pr^2 + \rho r^2 u^2)}{\partial r} = 2pr,$$

$$\frac{\partial(E r^2)}{\partial t} + \frac{\partial[r^2(p + E)u]}{\partial r} = 0, \qquad E = \rho\left(\varepsilon + \frac{u^2}{2}\right), \qquad p = \frac{(\gamma - 1)\rho\varepsilon}{1 - \rho b}. \tag{2}$$

Here r is the radial coordinate, p is the pressure, u is the velocity, ρ is the density, ε and E are the specific internal (per unit mass) and total (per unit volume) energies, $b = 1/\rho_{\max}$ ($\rho_{\max}$ is the maximum possible value of the gas density), and γ is the ratio of specific heats. The motion of the interface is described by the equation [9]

$$r_b \frac{du_b}{dt} + \frac{3}{2} u_b^2 = \frac{1}{\rho_f^0}(p_b - p_{\mathrm{ex}}) + \frac{r_b}{\rho_f^0 c_f^0} \frac{d}{dt}(p_b - p_{\mathrm{ex}}) + 4\nu\frac{u_b}{r_b}, \tag{3}$$

where r_b is the bubble radius, u_b is the velocity of the bubble surface, ρ_f^0 and c_f^0 are the density and speed of sound in the fluid, $p_b = p(r_b - 0, t)$ is the pressure on the bubble surface on the side of the gas, and ν is the kinematic viscosity. It is assumed that for $t = 0$ we have $p(r, 0) = p^0$, $\rho(r, 0) = \rho^0$, $u(r, 0) = 0$, and $0 \leqslant r \leqslant r_b^0 = r_b(0)$ (p^0 and ρ^0 are the initial undisturbed values of the gas pressure and density in the bubble).

The algorithm of solving problem (1)–(3) is based on the use of mixed Eulerian–Lagrangian coordinates ξ and τ. Substituting the variables $t = \tau$ and $r = r(\tau, \xi)$, we transform system (2) to

$$(q r^2 J)_\tau + (f r^2)_\xi = 2r J s,$$

where $q = (\rho, \rho u, E)^{\mathrm{t}}$, $f = q(u - r_\tau) + (0, p, pu)^{\mathrm{t}}$, $s = (0, p, 0)^{\mathrm{t}}$, and $J = \partial r/\partial \xi$ is the Jacobian of mapping; here and below the superscript t denotes transposition and the subscripts τ and ξ indicate the partial derivatives $\partial/\partial\tau$ and $\partial/\partial\xi$.

In calculations, the time axis is divided into layers τ^n ($n = 0, 1, 2, \ldots$), $\tau^0 = 0$, and $\tau^{n+1} = \tau^n + \Delta\tau^n$. At the time τ^n, the computational grid consists of the cells $[r_{i-1/2}^n, r_{i+1/2}^n]$, $r_{i+1/2}^n = r(\xi_{i+1/2}, \tau^n)$, $r_{1/2}^n = 0$, and $r_{I+1/2}^n = r_b(\tau^n)$, where $i = \overline{1, I}$, (I is the number of cells in the computational grid). The gas-dynamic parameters within one cell are assumed to be constant.

Let the values of the solution parameters in the cells at the layer τ^n be known. Their calculation at the layer τ^{n+1} begins with calculation of the pressure $p_{I+1/2}^n$ at the outer boundary of the gas bubble. This is done by using the relations of the problem of a flat piston moving into a tube ($u_b^n < u_I^n$) and out of the tube ($u_b^n > u_I^n$) with the velocity $u_{I+1/2}^n = u_b^n$ [11], the undisturbed parameters inside the tube being equal to their values in the Ith cell. After that we calculate the position of the outer boundary $r_{I+1/2}^{n+1} = r_{I+1/2}^n + \Delta\tau^n u_{I+1/2}^n$, determine the coordinates of the internal nodes of the computational grid $r_{i+1/2}^{n+1}$ using a prescribed law, calculate the velocities of the nodes $(r_\tau)_{i+1/2}^n = (r_{i+1/2}^{n+1} - r_{i-1/2}^{n+1})/\Delta\tau^n$, and calculate the mass, momentum, and total energy of the cells that refer to the later τ^{n+1} using the finite-difference scheme:

$$\frac{(q r^2 \Delta r)_i^{n+1} - (q r^2 \Delta r)_i^n}{\Delta\tau^n} + (f r^2)_{i+1/2}^n - (f r^2)_{i-1/2}^n = 2\tilde{r}_i^n \Delta r_i^n s_i^n.$$

Here $(ab)_i^n = a_i^n b_i^n$, $(r^2 \Delta r)_i^n = [(r_{i+1/2}^n)^3 - (r_{i-1/2}^n)^3]/3$, $f_{i+1/2}^n = f(q_{i+1/2}^n)$, $s_i^n = s(q_i^n)$, $(r^2)_{i+1/2}^n = [(r_{i+1/2}^n + \Delta r_{i+1/2})^3 - (r_{i+1/2}^n)^3]/(3\Delta r_{i+1/2})$, $\Delta r_{i+1/2} = (u - r_\tau)_{i+1/2}^n \Delta\tau^n$, $\tilde{r}_i^n = 0.5(\tilde{r}_{i-1/2} + \tilde{r}_{i+1/2})$, $\tilde{r}_{i+1/2} = [(r^2)_{i+1/2}^n]^{1/2}$, and $\Delta r_i^n = r_{i+1/2}^n - r_{i-1/2}^n$. To calculate the gas-dynamic parameters $q_{i+1/2}^n$, $u_{i+1/2}^n$, etc., which refer to the cell boundary, we solve the Riemann problem for a discontinuity formed by different values of the parameters in the cells i and $i + 1$. The sought values are the solution of this problem at the point $r_{i+1/2}^{n+1}$.

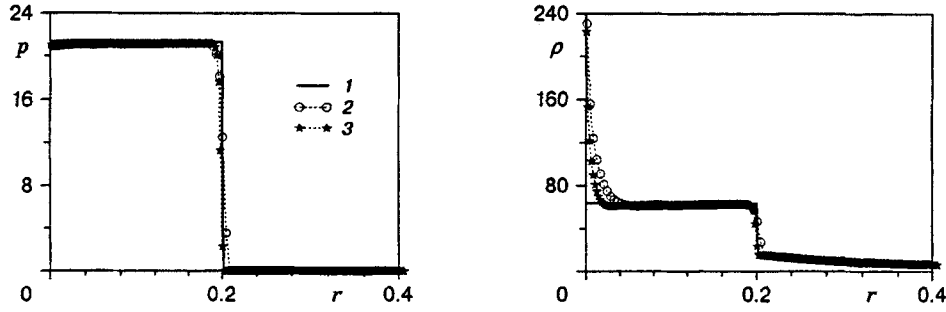The calculation at the layer τ^{n+1} is finished by determining the velocity of the outer boundary of the

Fig. 1

bubble u_b^{n+1} in accordance with Eq. (3). Prior to each next step, we determine its magnitude

$$\Delta\tau^n = \alpha_C \min_{1\leqslant i\leqslant I} \left\{ \frac{\Delta r_i^n}{\max(|u_{i-1/2}^n - (r_\tau)_{i-1/2}^n + c_{i-1/2}^n|, \ |u_{i+1/2}^n - (r_\tau)_{i+1/2}^n - c_{i+1/2}^n|)} \right\},$$

where α_C is the Courant number and $c_{i+1/2}^n$ is the local speed of sound.

Solution of the Problem of Motion of a Cold Gas to a Point [3]. At $t = 0$, a uniform gas with the parameters ρ^0 and $p^0 = 0$ moves to the pole of a spherical system of coordinates with the velocity $u^0 < 0$, which is equal everywhere. We have to find the distribution of the parameters along r for $t > 0$. The structure of the solution is such that for $t > 0$ there are two zones separated by a shock wave propagating from the pole with a constant velocity $D > 0$. The values of the parameters at the interface obey the Hugoniot relations, and at an infinitely distant boundary we have $\rho(\infty, t) = \rho^0$, $p(\infty, t) = 0$, and $u(\infty, t) = u^0$. For the equation of state $p = (\gamma - 1)\rho\varepsilon$, the solution has the form

$$\varepsilon = (u^0)^2/2, \quad \rho = \rho^0(1 - u^0/D)^3, \quad u = 0 \quad \text{for} \quad r < Dt;$$

$$\varepsilon = 0, \qquad\quad \rho = \rho^0(1 - u^0/D)^2, \quad u = u^0 \quad \text{for} \quad r > Dt,$$

where $D = -(\gamma - 1)u^0/2$.

The calculation results obtained on a uniform moving grid are shown in Fig. 1. This is a spatial distribution of the parameters at the time $t = 0.6$. The following input data are used in the problem: $\gamma = 5/3$, $\rho^0 = 1$, $u^0 = -1$, and $\alpha_C = 0.356$. The computational domain for $t = 0$ is the interval $0 \leqslant r \leqslant 1$. The motion of the grid is determined by the displacement of the right boundary with the velocity u^0. Curves 1 refer to the analytical solution, and curves 2 and 3 show the numerical solution (curves 2 were obtained on a grid of 100 cells, curves 3 on a grid of 200 cells).

The calculated curves for pressure (and velocity) are in good agreement with the analytical data. At the same time, there is a significant difference in density (and internal energy) near the pole. For example, the density in the cells adjacent to the pole, which was obtained on a grid of 100 cells, exceeds the exact value by more than a factor of 3.5.

The numerical solution of this problem by another difference method is discussed [13], where the calculated profile of density near the pole deviates strongly from the exact value, but downwards rather than upwards, as in Fig. 1. To improve the agreement with the exact solution, Noh [13] proposes to decrease the numerical viscosity and introduce an artificial heat flux. Taking into account the behavior of the calculated density profiles in Fig. 1 obtained without artificial viscosity, we can expect that the introduction of artificial viscosity is quite reasonable.

Various variants of artificial viscosity were tested. The best results were obtained using the modification of the second equation of system (2)

$$\frac{\partial(\rho r^2 u)}{\partial t} + \frac{\partial(pr^2 + \rho r^2 u^2)}{\partial r} = 2pr + 2r(\tau^{rr} - \tau^{\varphi\varphi}),$$
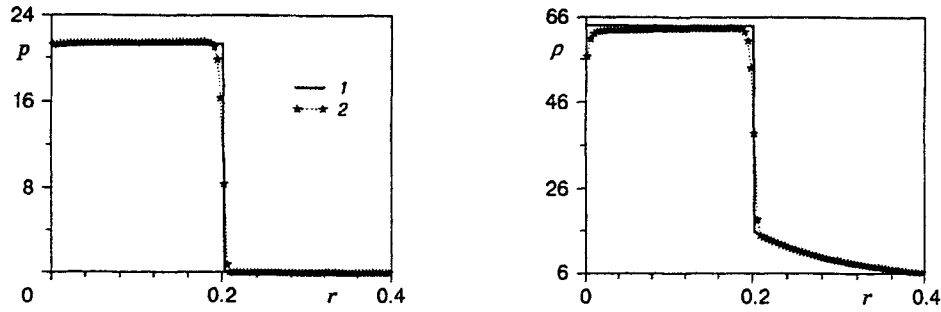
Fig. 2

$$\tau^{rr} - \tau^{\varphi\varphi} = 2\mu\left(\frac{\partial u}{\partial r} - \frac{u}{r}\right), \qquad \mu = \begin{cases} (k_\mu l)^2 \dfrac{\partial u}{\partial r} & \text{for} \quad \dfrac{\partial u}{\partial r} < 0, \\[2mm] 0 & \text{for} \quad \dfrac{\partial u}{\partial r} \geqslant 0, \end{cases}$$

where k_μ is a dimensionless coefficient and l is a parameter with the dimension of length. Passing to the mixed Eulerian–Lagrangian variables, we obtain

$$(\rho u r^2 J)_\tau + [\rho r^2 u(u - r_\tau) + pr^2]_\xi = 2rJp + 2rJ(\tau^{rr} - \tau^{\varphi\varphi}),$$

$$\tau^{rr} - \tau^{\varphi\varphi} = 2\mu\left(\frac{1}{J} u_\xi - \frac{u}{r}\right), \qquad \mu = \begin{cases} (k_\mu l)^2 \rho \dfrac{1}{J} u_\xi & \text{for} \quad u_\xi < 0, \\[2mm] 0 & \text{for} \quad u_\xi \geqslant 0. \end{cases}$$

In the numerical realization, we accept

$$(\tau^{rr} - \tau^{\varphi\varphi})_i^n = 2\mu_i^n\left(\frac{1}{\Delta r_i^n}\Delta u_i^n - \frac{u_i^n}{r_i^n}\right), \qquad \mu_i^n = (k_\mu \Delta r_i^n)^2 \rho_i^n \frac{1}{\Delta r_i^n}\Delta u_i^n,$$

where $\Delta u_i^n = u_{i+1/2}^n - u_{i-1/2}^n$. The optimal values of the coefficient k_μ were chosen in the course of calculations.

Figure 2 shows the calculation results obtained on a grid of 100 cells for $k_\mu^2 = 0.067$ (the remaining parameters are the same as in Fig. 1). The introduction of terms with artificial viscosity made the numerical solution much closer to the analytical result. The character of the curves is also different: when approaching the pole, the density decreases (the internal energy increases). The calculations show that the decrease in density and the increase in internal energy near the pole become more significant as k_μ increases. Note that closer agreement between the numerical and analytical solutions can be achieved by using an artificial heat flux [11].

Solution of the Problem of a Spherical Piston Converging to a Point. At $t < 0$ the spherical piston is at rest at the point $r = r^0$. A perfect gas with the parameters γ, ρ^0, and c^0, which is enclosed inside the volume limited by the piston, is also at rest ($u^0 = 0$). It is assumed that $p = (\gamma - 1)\rho\varepsilon$. At $t = 0$ the piston instantaneously starts its motion toward the pole with a constant velocity $u_p < 0$. A shock wave arises near the piston, and the shock-wave strength increases as it approaches the pole. Being focused at the pole, the shock wave reflects from it and propagates in the opposite direction.

When there is a converging or diverging shock wave in a small vicinity of the pole, this problem has a self-similar character [14]. Prior to focusing of the converging shock wave in this region, we have

$$|u| \sim r^{-(1/\beta - 1)}, \qquad \rho = \text{const}, \qquad p \sim r^{-2(1/\beta - 1)}, \qquad \varepsilon \sim r^{-2(1/\beta - 1)}, \tag{4}$$

where β is a factor of self-similarity. For $\gamma = 1.4$, we have $\rho^*/\rho^0 = 20.1$ and $\beta = 0.7172$ (ρ^* is the gas density behind the shock-wave front at the time of its focusing). In addition [9], $\rho_2^*/\rho_1^* = 2.3$ (ρ_1^* and ρ_2^* are the gas densities in front of and behind the front of the diverging shock wave).

Figure 3 shows the spatial distributions of the parameters for the following input data: $\gamma = 1.4$, $\rho^0 = 1$,
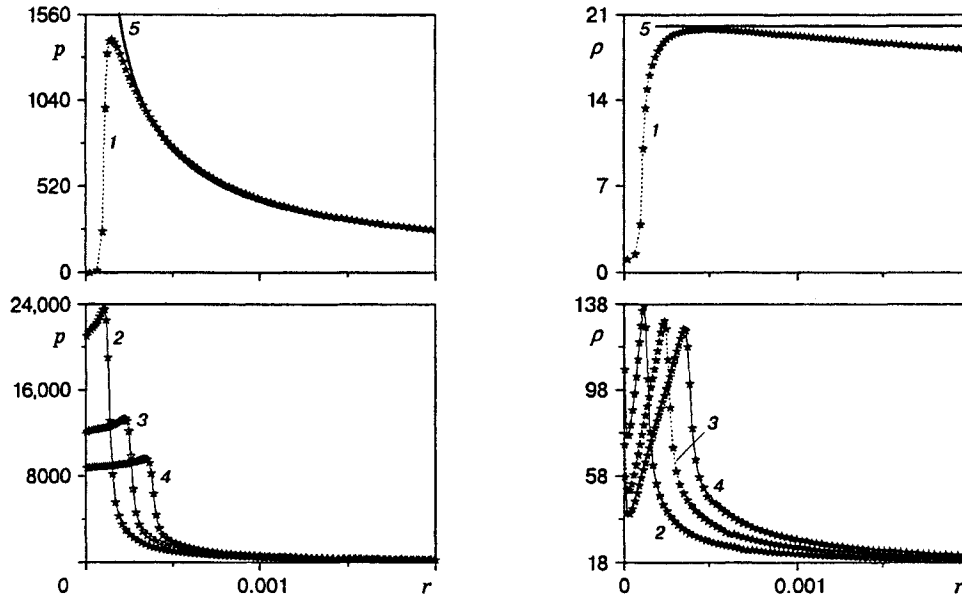
Fig. 3

$c^0 = 1$, $u_p = -0.5$, $k_\mu^2 = 0.067$, and $\alpha_C = 0.35$ (c^0 is the undisturbed speed of sound). At the initial time $t = 0$, the computational domain $0 \leqslant r \leqslant 1$ was covered by a computational grid of 800 cells, which condensed toward the pole in accordance with the geometric progression. The size of the cell adjacent to the pole was $5 \cdot 10^{-5}$. The Lagrangian coordinate system was used ($r_\tau = u$).

The calculated curves in Fig. 3 refer to the time $t_1 \approx 0.5928775$ close to the moment of shock-wave focusing in the pole (curves 1) and three times soon after the focusing: $t_2 = 0.5928889$, $t_3 = 0.5929008$, and $t_4 = 0.5929147$ (curves 2–4). Curves 5 are plotted for the time t_1 in accordance with Eqs. (4). A scale factor was used to construct the pressure curve. This factor was calculated on the basis of the numerical solution at the center of one of the computational cells (at the point $r \approx 3.89 \cdot 10^{-4}$). The following criteria were used to choose the appropriate cell: 1) the cell was located behind the shock-wave front; 2) the cell was as close to the pole as possible; 3) the density in this cell was found in the region $\rho = const$.

The agreement between the numerical and analytical curves at the time t_1 is quite satisfactory. The disagreement on the left of the point of their intersection is explained by numerical smearing of the shock-wave front, and the discrepancy on the right of this point is related to the fact that the solution of the problem deviates more and more from the self-similar result with increasing distance from the shock-wave front. For density curves at the times t_2–t_4 at the shock-wave front, the ratio ρ_2^*/ρ_1^* is roughly equal for all curves and amounts to 2.2, which is also in good agreement with the value of 2.3 [9]. The increase in density and the decrease in internal energy, which is not plotted in Fig. 3, described in the previous problem are observed near the pole. These effects are reduced by using artificial viscosity. Special calculations for choosing the optimal coefficients of artificial viscosity k_μ were not performed in this problem.

Gas Dynamics During the Collapse of a Bubble Located in a Weakly Compressible Fluid. The problem was solved for the following input data: $\gamma = 1.4$, $r_b^0 = 4.5 \cdot 10^{-6}$ m, $u_b^0 = 0$, $T^0 = 300$ K, $k_\mu^2 = 0.067$, $p^0 = 1.01 \cdot 10^5$ Pa, $c_f^0 = 1500$ m/sec, $\rho_f^0 = 967.95$ kg/m^3, $\nu = 0.7 \cdot 10^{-5}$ m^2/sec, and $\omega = 2\pi \cdot 26.5$ kHz. The temperature T was calculated from the relation $T = (1/\rho - b)p/R'$, where $b = 1/794$ m^3/kg and $R' = 287$ J/(kg·K). To estimate the influence of different methods of solution, the initial values were chosen close to those used by Wu and Roberts [9].

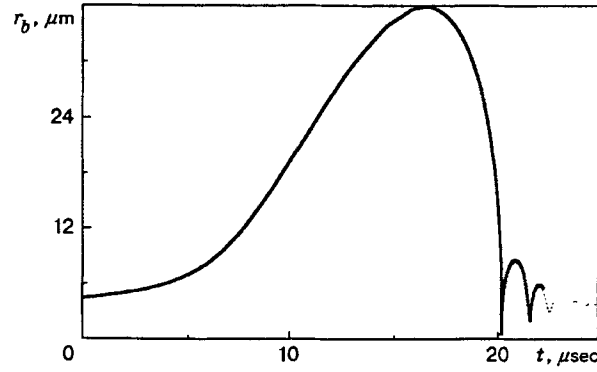For comparison, we use the results for this problem calculated under the assumption that the gas

Fig. 4

expansion–compression in the bubble occurs uniformly. In this case, we have

$$p_b = p_b^0[(r_b^0)^3 - a^3]^\gamma(r_b^3 - a^3)^{-\gamma}, \qquad a = r_b^0(\rho_b^0 b)^{1/3}. \tag{5}$$

Figure 4 shows the time dependence of the bubble radius r_b within the interval $0 \leqslant t \leqslant 25$ μsec. The solutions of Eq. (3) together with relation (5) and system (2) coincide in the graph. In the initial stage, when the bubble radius increases to its maximum value $r_{b\ max}$ (expansion phase), the solutions coincide within the framework of both formulations; therefore, to decrease the computer time, the calculation in this interval is performed on a grid consisting of two cells with an equal size at $t = 0$. The calculation is performed in the Lagrangian coordinates ($r_r = u$), $\alpha_C \approx 0.12$. When the bubble radius reaches the maximum value, a conservative interpolation of the solution to a new uniform grid consisting of 370 cells is performed.

In the solution of Eq. (3) together with (5), the maximum value of the bubble radius $r_{b\ max} = 35.91$ μm is reached at $t = 16.606$ μsec; at this moment, $p \approx 16.46$ Pa, $\rho \approx 0.0023$ kg/m^3, and $T \approx 24.8$ K. The minimum value of the bubble radius $r_{b\ min} = 0.566$ μm is reached at $t \approx 20.229175$ μsec; at this moment, $p \approx 41 \cdot 10^8$ Pa, $\rho \approx 590.1$ kg/m^3, and $T \approx 6214$ K.

In the solution of Eq. (3) together with system (2), $r_{b\ min} = 0.5465$ μm is reached at $t \approx 20.211275$ μsec. At the center of the bubble we have $p \approx 82.47 \cdot 10^8$ Pa, $\rho \approx 32.88$ kg/m^3, and $T \approx 837655$ K.

Figure 5 shows the spatial distributions of the gas parameters for 15 times: $t_k = 20.211 + t_k^*$ ($k = \overline{1, 15}$), where $t_1^* \approx 0.241$, $t_2^* \approx 0.243$, $t_3^* \approx 0.250$, $t_4^* \approx 0.252$, $t_5^* \approx 0.257$, $t_6^* \approx 0.360$, $t_7^* \approx 0.390$, $t_8^* \approx 0.410$, $t_9^* \approx 0.430$, $t_{10}^* \approx 0.450$, $t_{11}^* \approx 0.455$, $t_{12}^* \approx 0.470$, $t_{13}^* \approx 0.490$, $t_{14}^* \approx 0.520$, and $t_{15}^* \approx 0.560$ (t_k^* is the parameter that specifies the time step in microseconds). The curve numbered by k corresponds to the time t_k.

As the bubble radius decreases from $r_{b\ max}$ to $r_{b\ min}$, the velocity of its surface and the gas particles inside the bubble increases more and more and becomes supersonic inside the bubble at $t \approx 20.2112$ μsec at the point $r \approx 0.3$ μm. The surpassing of the local speed of sound gives rise to a shock wave whose strength rapidly increases when approaching the pole (curves 1–3). At the time t_3, the shock wave is located in the immediate vicinity of the pole. During the shock-wave focusing, the pressure, velocity, and temperature behind the front are limited in calculations because of the finite size of the computational cells; the value of density is limited by constraints imposed by the van der Waals equation of state.

After the focusing of the converging shock wave in the pole, a diverging shock wave arises, which propagates in the opposite direction to the bubble surface (curves 4–6). In the vicinity of the pole ($r < 0.05$ μm), the gas remains strongly heated, and the density in this region is lower than in the periphery.

In the interval $t_6 < t < t_7$, the shock wave interacts with the bubble surface, which results in the appearance of an expansion wave moving away from the interface between the phases (curves 7 and 8). As the expansion wave moves to the pole, the second shock wave arises (curves 9 and 10). After its focusing in the pole, the second diverging shock wave appears, which propagates to the outer boundary of the bubble (curves 11–15).

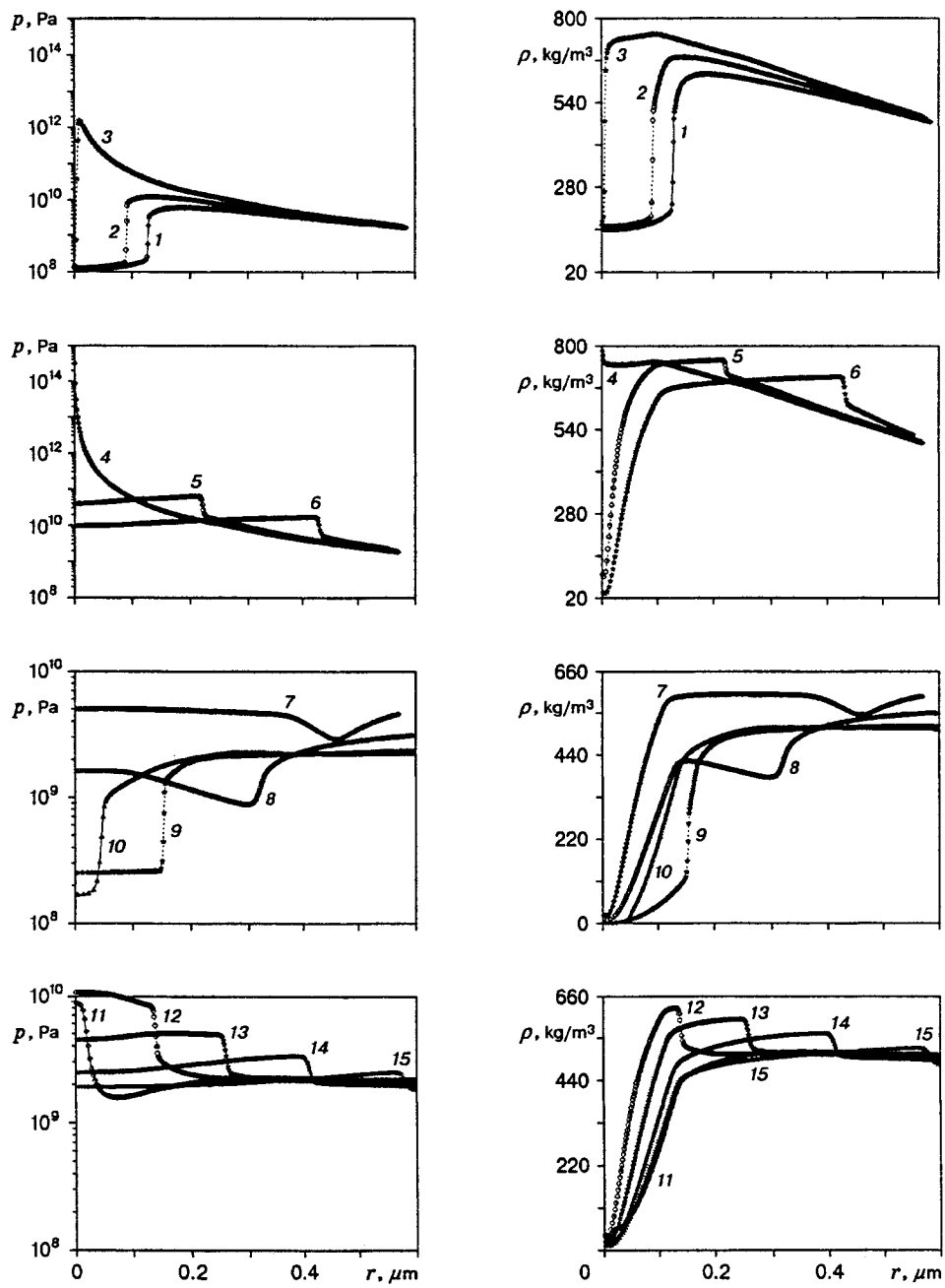The appearance and propagation of the converging and diverging shock waves within the time interval
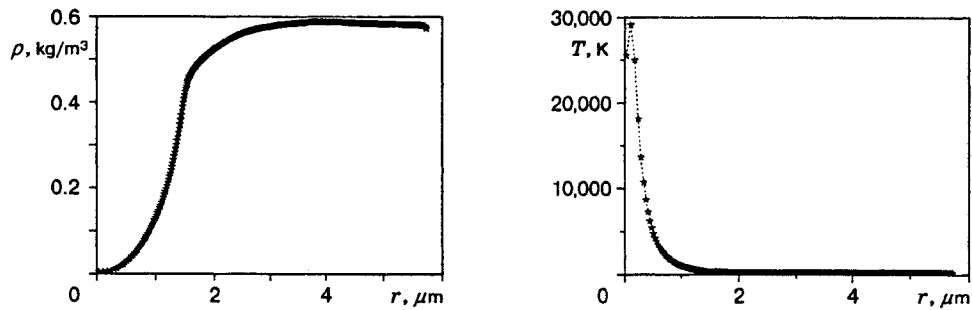
Fig. 5

282

Fig. 6

$t_1 \leqslant t \leqslant t_6$ are repeated to a large extent within the interval $t_7 \leqslant t \leqslant t_{15}$. At the same time, the changes in the gaseous medium of the bubble, which took place within the interval $t_1 \leqslant t \leqslant t_6$, make the shock waves much weaker in the second case.

Figure 6 shows the spatial distributions of the parameters for $t \approx 22.18149$ μsec, when the intense processes of bubble collapse are completed. The pressure is constant $(0.41 \cdot 10^5$ Pa), but great changes in density and temperature are observed: within the range $r < 2$ μm, the density decreases and the temperature increases. This behavior of the parameters is explained by irreversible processes that occur in passing of the shock waves.

The results in Figs. 4 and 5 agree qualitatively with the data [9]. As a whole, we obtain a reasonable description of the shock waves, which are clearly visible in the graphs of spatial distributions of the parameters (see Fig. 5). The temperature curves (see Fig. 6) have a weakly noticeable decrease at the point near the pole, the corresponding peak in the density profiles cannot be distinguished because of the scale used. This behavior is the manifestation of the numerical effects considered above in the problem of motion of a cold gas to a point. These effects could be substantially reduced by using artificial viscosity.

Conclusion. The specific features of numerical simulation of gas dynamics in a bubble in the phase of its collapse with the formation of shock waves are considered. The problems of motion of a cold gas to a point and a spherical piston converging to a point are used to evaluate the algorithm. In the first problem, it is shown that significant errors can arise in the vicinity of the pole if special measures are not taken. These errors can be substantially reduced by means of artificial viscosity in the Riemann problem. In the second problem, the self-similar regime is reached, which verifies the correctness of the numerical solution. The problem of gas dynamics in a bubble during its collapse in a weakly compressible fluid has been considered. Qualitative agreement of the results obtained with the known solution is observed. The errors of the numerical solution near the pole are significantly reduced by using artificial viscosity.

REFERENCES

1. Lord Rayleigh, "On the pressure developed in a liquid during the collapse of a spherical cavity," *Philos. Mag.*, **34**, No. 200, 94–98 (1917).
2. M. S. Plesset, "The dynamics of cavitation bubbles," *J. Appl. Mech.*, **16**, 277–282 (1949).
3. R. I. Nigmatulin, *Dynamics of Multiphase Media*, Part 1, Hemisphere Publ., New York (1991).
4. D. F. Gaitan, L. A. Crum, R. A. Roy, and C. C. Church, "Sonoluminescence and bubble dynamics for a single, stable cavitation bubble," *J. Acoust. Soc. Amer.*, **91**, 3166–3172 (1992).
5. L. A. Crum, "Sonoluminescence, sonochemistry, and sonophysics," *J. Acoust. Soc. Amer.*, **95**, No. 1, 559–562 (1994).

6. R. Löfstedt, B. P. Barber, and S. J. Putterman, "Towards a hydrodynamic theory of sonoluminescence," *Phys. Fluids*, **5**, No. 11, 2911–2928 (1993).

7. R. I. Nigmatulin, V. Sh. Shagapov, N. K. Vakhitova, and R. T. Lékhi, Jr., "Method of superstrong compression of a gaseous bubble in a fluid by nonperiodic vibrations of moderate-amplitude pressure," *Dokl. Ross. Akad. Nauk*, **341**, No. 1, 37–41 (1995).

8. R. I. Nigmatulin, I. Sh. Akhatov, and N. K. Vakhitova, "Compressible fluid in gas bubble dynamics," *Dokl. Ross. Akad. Nauk*, **348**, No. 6, 768–771 (1996).

9. C. C. Wu and P. H. Roberts, "Shock wave propagation in a sonoluminescencing gas bubble," *Phys. Rev. Lett.*, **70**, 3424–3427 (1993).

10. L. Kondic, J. I. Gersten, and C. Yuan, "Theoretical studies of sonoluminescence radiation: Radiative transfer and parametric dependence," *Phys. Rev. E*, **52**, 4976–4990 (1995).

11. A. A. Aganin and M. A. Il'gamov, "Specific features of calculation of nonlinear spherical waves using the Riemann problem," in: *Modeling of Dynamic Processes in Continuum Media* (collected scientific papers) [in Russian], Izd. Kazan' Mat. Ob., Kazan' (1997), pp. 108–193.

12. W. C. Moss, D. B. Clarke, J. W. White, and D. A. Young, "Hydrodynamic simulations of bubble collapse and picosecond somoluminescence," *Phys. Fluids*, **6**, No. 9, 2979–2985 (1994).

13. W. F. Noh, "Errors for calculations of strong shocks using an artificial viscosity and an artificial heat flux," *J. Comput. Phys.*, **72**, 78–120 (1978).

14. L. D. Landau and E. M. Lifshits, *Theoretical Physics*, Vol. 4: *Hydrodynamics* [in Russian], Nauka, Moscow (1988).